Correspondence to:
L. G. Lanza,
luca.lanza@unige.it

Wind Tunnel Validation of a Particle Tracking Model to Evaluate the Wind-Induced Bias of Precipitation Measurements

A. Cauteruccio[1] , E. Brambilla[2] , M. Stagnaro[1] , L. G. Lanza[1,3] , and D. Rocchi[2]

[1]Department of Civil, Chemical and Environmental Engineering, University of Genova, Genoa, Italy, [2]Department of Mechanical Engineering, Politecnico di Milano, Milan, Italy, [3]WMO/CIMO Lead Centre "B. Castelli" on Precipitation Intensity, Genoa, Italy

Abstract A physical full-scale experimental set-up was designed and implemented in the wind tunnel to reproduce and capture the trajectories of falling water drops when approaching the collector of catching type precipitation gauges, reproducing rainfall measurements in windy conditions. The experiment allowed to collect, for the first time, a large data set of high-resolution footages of the deviation of such trajectories, as induced by the bluff-body aerodynamics of the outer gauge shape. By processing the collected images, a consistent quantitative interpretation of each drop pattern was possible, based on a detailed Computational Fluid Dynamics simulation of the airflow updraft and acceleration features above the collector of the gauge. Numerical airflow simulations were extensively validated in the wind tunnel, using local flow measurements and Particle Image Velocimetry. Capturing the deviation of the drop trajectories in the wind tunnel allowed a clear visualization of the physical reason for the wind-induced undercatch of precipitation gauges, since drops were individually observed to fall outside instead of inside of the collector, contrary to what would be expected by extrapolating their undisturbed trajectory. The adopted Lagrangian Particle Tracking model and the formulation used for the drag coefficient were suitable to closely reproduce the observed drop trajectories when affected by the airflow deformation due to the bluff-body aerodynamics of two investigated gauge geometries. The wind tunnel experiment provided the basis for the validation of the particle tracking model in terms of the difference between simulated and observed trajectories, after initial conditions were suitably set to represent the experimental setup.

1. Introduction

The wind-induced undercatch of precipitation gauges is defined as the reduced amount of precipitation captured by the collector of the gauge with respect to the amount that would be captured if the gauge were transparent to the wind. When the gauge is exposed to the wind, airflow deformations occur above and upwind of the collector due to the bluff-body aerodynamics of the gauge outer geometry. Significant acceleration and vertical velocity components are generated (see e.g., Jevons, 1861; Warnik, 1953), inducing some deformation of the fall trajectories of the approaching hydrometeors and generally resulting in a lower collection of precipitation than in the absence of wind.

Instrumental measurement biases for precipitation gauges, well described and addressed in the literature (see e.g., La Barbera et al., 2002; Molini et al., 2005; Valík et al., 2021), propagate through the applications or the modeling chain (Habib et al., 2008) and their awareness is often rapidly lost, yielding limited reliability of the obtained results (Lanza & Stagi, 2008). Similar implications to real-world hydrological applications are expected for the wind-induced undercatch.

Adjustments for the wind-induced bias are traditionally derived from field experiments, where the ratio between the precipitation amount measured by the gauge and a suitable reference configuration with limited exposure to the wind is used as a measure of the Collection Efficiency (CE). This is a function of the wind speed at the collector's height and of further influencing variables, such as the microphysical characteristics of the precipitation events at the field test site. The choice of the influencing variables adopted to derive best-fit adjustment curves from the field-measured data affects the representativeness of the results and their transferability to any different site climatology and gauge configuration. This also reflects into

a generally large spread of the residuals around the derived adjustment curves because a comprehensive parameterization based on all the influencing variables is difficult to achieve.

Most recent advances in the literature are concentrated on a physically based numerical approach to supplement experimental studies. CE curves for both liquid (see Cauteruccio & Lanza, 2020) and solid (Cauteruccio, Chinchella, et al., 2021) precipitation are derived as a function of the precipitation intensity, particle size distribution, and wind speed. The numerical approach, after proper validation, allows to investigate various gauge shape/precipitation type combinations, subject to the desired wind and precipitation climatology.

The numerical approach is based on Computational Fluid Dynamics (CFD) simulations of the airflow field surrounding the gauge body (see e.g., Colli et al., 2018) and a Lagrangian Particle Tracking (LPT) model to evaluate the airflow induced deformation on the trajectory of the approaching hydrometeors (see e.g., Nešpor & Sevruk, 1999).

The work of Mueller and Kidder (1972) is among the earliest studies on the modeling of hydrometeor trajectories using a LPT model; in that work, particle trajectories were numerically simulated based on the flow field measured in the wind tunnel (WT) employing hot film anemometers. Folland (1988) later developed two simplified trajectory models to estimate the catch losses due to the wind. They were based on flow patterns (flow velocity and direction) obtained in the vertical section along the symmetry axis in the streamwise direction partially published by Robinson and Rodda (1969), and the flow field close to the windward edge as described in the work of Warnik (1953). In the first model, a two-dimensional solution was obtained by simulating one by one drops of fixed diameter until the expected drop size distribution was generated. Then the model was extended to a three-dimensional domain by considering the variation of the gauge orifice width in the transversal direction. The second model, which the author terms "semi-analytical", uses geometrical considerations to calculate the number of particles which fall outside instead of inside of the gauge collector.

In the work of Nešpor and Sevruk (1999), the airflow velocity field around three cylindrical gauges characterized by different shapes of the collector rim was calculated by numerically solving the Reynolds Average Navier-Stokes (RANS) equations based on the k-ε turbulence closure model where k is the turbulence kinetic energy and ε the energy dissipation per unit mass. Then, liquid particle trajectories were modeled by employing a one-way coupled model where spherical particles are separately simulated for each diameter and the CE is evaluated by computing the integral, over the particle size distribution, of the number of particles collected by the gauge with respect to the total precipitation. This simulation scheme was also adopted by Thériault et al. (2012) and Colli et al. (2015; 2016a, 2016b) for solid precipitation, by increasing the details of the computational mesh to better capture the airflow features and using also Large Eddy Simulations (LES).

In the work of Thériault et al. (2012) different crystal types were modeled by using a power law parametrization of the terminal velocity, volume, density, and cross section of the particles, while Colli et al. (2016b) investigated two macro categories: wet and dry snow as suggested by Rasmussen et al. (1999). In these works, a fixed drag coefficient for each crystal type was adopted. In the work of Colli et al. (2016b), the obtained CE curves for the two macro categories act as upper and lower thresholds of the wide spreading of experimental data.

Colli et al. (2015) obtained a better comparison with real-world data by introducing the dependence of the aerodynamic Drag Coefficient (C_D) on the local Reynolds number of the simulated particle (Re_p). The Re_p is function of the instantaneous particle-to-air magnitude of velocity and the particle trajectory is obtained by updating its value and the associated C_D at each simulation time step.

In the present work the improved LPT model used by Colli et al. (2015) for solid precipitation was adapted to simulate the trajectories of water drops when falling through the atmosphere and approaching the gauge collector, using suitable C_D equations as a function of the Re_p. Various equations were implemented for different Re_p ranges derived from literature formulations and data.

Due to the difficulties in reproducing hydrometeors trajectories under controlled WT conditions, or to observe their deflection when approaching the gauge in any real world configuration, the validation of trajectory models is scarcely documented yet in the literature. Very few works in the literature, Warnik (1953) and Green and Helliwell (1972), report some attempts to detect water drops in the WT.
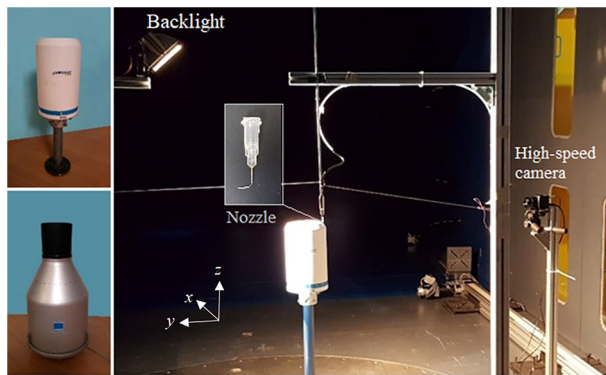
Figure 1. Lambrecht Rain(e)H3$^©$ (top-left) and Geonor T200 B$^©$ (bottom-left) precipitation gauges and experimental setup used to release drops and photograph their trajectories as installed in the GVPM (wind is along the x direction).

The WT experiment performed by Warnik ([1953](#)) was a pioneering work, where the trajectories of solid particles under windy conditions and their deviations when approaching the gauge were first visualized. However, no attempt to quantitatively measure and model the deviation of particles in the presence of the gauge collector was made and just the overall undercatch was quantitatively obtained. The main objective was to define the air-flow behavior around the investigated gauges and to give definite information about the inconsistencies observed in records of snow catch in precipitation gauges. Results were used to design the geometry of two windshields with better performance than the shields in use at that time.

Green and Helliwell ([1972](#)) measured wind velocity profiles and raindrop trajectories above a cylindrical rain gauge in a WT. The flow field was measured using a grid of hotwire anemometers and the trajectories of injected drops using photographs from a still reflex camera. They simulated the drop trajectories based on the streamlines obtained by visually interpreting the pattern of smoke injected in the WT. Little details are however provided about the algorithms and procedures used in that work.

The original contribution of the present work consists of a dedicated WT experimental setup, where a physical full-scale model was designed and realized to release water drops in the flow field and to detect—at high resolution—their deviated trajectories close to the gauge collector, where the airflow field is modified by the presence of the gauge body. Various wind speed and fall height combinations were tested in a controlled WT environment. Flow velocity measurements were obtained by employing a multi-hole probe and a Particle Image Velocimetry (PIV) technique.

The objective of the present work is the validation in the WT of the modeling chain composed of CFD simulations—to establish the airflow patterns (acceleration, velocity components and turbulence intensity) produced by the aerodynamic response of the gauge geometry—and LPT algorithm—to assess the one-way coupled airflow-raindrop interaction.

2. Methodology

The most popular outer shapes of catching type precipitation gauges, cylindrical (hereinafter CY) and chimney (CH), were investigated. Although actually exploiting a weighing measurement principle, the Lambrecht Rain(e)H3$^©$ precipitation gauge has a cylindrical outer shape with collector diameter $D = 0.16$ m and height $h = 0.307$ m (see Figure [1](#) top-left) and is assumed here as representative of the majority of tipping-bucket gauges, while the Geonor T200B$^©$ (with the same D and $h = 0.740$ m) has a chimney shape (see Figure [1](#) bottom-left), as is typical of many weighing-type gauges.

Within the PRIN 20154WX5NA project "Reconciling precipitation with runoff: the role of understated measurement biases in the modeling of hydrological processes," an extensive experimental campaign was conducted in the WT of the DICCA department at the University of Genova and in the WT facility available at Politecnico di Milano, hereafter GVPM. This includes flow velocity measurements obtained by using a multi-hole probe (employed in the DICCA WT), as well as Particle Image Velocimetry (PIV) and a dedicated technique designed to release and track water drops using a drop generator and a high-speed camera (employed in the GVPM).

Dedicated numerical simulations of the experimental setup were performed with suitable initial conditions (drop velocity and position), as observed in the WT. The comparison between CFD airflow fields and velocity measurements and between the simulated and observed drop trajectories led to the validation of the whole numerical approach.

In both the simulations and the reported observations, the three Cartesian coordinates are set with the x axis orientated along the streamwise direction, the y axis along the crosswise direction and the z axis along the upward vertical direction, as shown in Figure [1](#).

2.1. Wind Tunnel Experiments

The DICCA WT has a working chamber of length of 8.8 m and cross area of 1.7×1.35 m^2 (width $\times$ height), while the GVPM has a low turbulence-high speed chamber of $4 \times 4 \times 4$ m^3. In both facilities the gauge collectors were positioned at 1 m from the floor and in the center of the cross section to avoid any interaction with the surrounding walls. The boundary layer develops in about 0.10 m from the floor and all tests were conducted under low turbulence conditions (turbulence intensity $I_{turb} \approx 0.5\%$) and uniform-constant incoming wind.

The Lambrecht Rain(e)H3$^{©}$ precipitation gauge (hereinafter CY gauge) was tested in the DICCA WT. Measurements of the wind speed were acquired using a fast-response multi-hole probe, the "Cobra" probe, characterized by a measuring cone of $\pm 45°$, mounted on a traversing system with three degrees of freedom. Each measurement was sampled at 2 kHz for 30 s. The measurement positions were selected above the gauge along two longitudinal profiles at different elevations and along two vertical profiles at the center and the upwind edge of the collector.

The Geonor T200B$^{©}$ precipitation gauge (hereinafter CH gauge) was tested in the GVPM using the PIV technique. The test chamber was uniformly filled with castor oil smoke, used as a tracer. A laser emitter was mounted on the ceiling of the test chamber to illuminate the measurement plane, while the surrounding environment was kept in the dark. The video camera was positioned with its central axis normal to the streamwise direction (x) and centered on the gauge collector. Post processing of the acquired images provided the flow velocity field discretized in a regular grid with cell size of 7.5×7.5 mm. Part of the data, acquired very close to the gauge surface and disturbed by the reflection of the laser beam on the gauge rim, were masked out.

With the aim to validate the LPT model, water drops were injected in the GVPM and their trajectories were captured with a high-speed camera in the vertical 2-D plane (x, z) along the main flow direction. The deviation of the drop trajectories approaching and traveling above the gauge collector was measured. The WT was equipped with a hydraulic system and a high-power lamp to generate and illuminate drops along their trajectories. The experimental setup is illustrated in the right-hand panel of Figure 1.

The hydraulic system consisted of a tank with a constant water head, feeding a volumetric pump (Ismatec Reglo-CPF digital) connected to a calibrated nozzle; the drops releasing frequency could be adjusted by varying the pump flow rate between 0.4 and 18.0 ml/min. Tests were conducted using a fixed flow rate of 0.8 ml/min and a nozzle orifice size of 0.008''. The support for the nozzle was shaped to have a reduced impact on the airflow close to the orifice and to minimize the oscillations at the edge where drops are released. The releasing position was fixed at about five diameters upstream of the upwind edge of the collector along the streamwise symmetry axis of the gauge (x direction).

The high-speed camera was placed in front of the gauge (as described above for the PIV measurements) and its distance from the gauge collector was optimized to increase the resolution of the captured drop images without affecting the airflow field near the target. The focus plane was set as the vertical section along the streamwise symmetry axis of the gauge collector (x direction). Acquisition of video sequences was carried out at both a high and a low frame rate (fps). In the first case, the recording speed was optimized to maintain high quality of the images, in terms of resolution and luminosity, suitable for capturing the drop movement with no streaks appearing due to an excessive exposure time with respect to the drop displacement. The recording speed was set to 1,000 fps, with an image resolution of $1,600 \times 900$ pixels. During the low frame rate acquisition, the recording speed was kept low, 10 fps with the same image resolution, in order to increase the exposure time. In this way the trajectory of a bright moving object was imprinted in a single image in the form of a streak.

The lighting was designed to increase the visibility of drops in the video: an incandescent lamp was used to illuminate the volume near the gauge collector. Tests were conducted in a dark environment while backlighting the gauge from above using the lamp. The lamp lights are suitably directed to avoid the saturation of the recorded videos.

The GVPM campaign was realized in subsequent time slots, in each of them the dimension of the image was about 40×20 cm with the pixel size equal to 0.2370 mm for the CH gauge and 0.2424 mm for the CY

gauge. The wind speed range investigated was between 9 and 13 m s^{-1} to appreciate the deformation of the drop trajectories when the flow field is disturbed by the presence of the gauge.

The drop release position was determined a priori using the LPT model based on the flow field provided by CFD simulations at a wind speed equal to 10 m s^{-1}. Simulations were run by setting the drop size equal to the minimum dimension that the video camera is able to capture (1 mm) following dedicated tests performed in still air and the initial velocity of the drop was imposed equal to zero in all directions according to the releasing system. This configuration allowed a significant deformation of the trajectories to be observed when drops traveled in the region where the flow field is disturbed by the presence of the gauge.

During the experiment drops of diameter between 0.7 and 1.2 mm were generated. The drop size/ wind speed configuration was chosen since drops could not be generated with their terminal velocity, otherwise—given the above-mentioned constraints on the drop size—the high inertia of such large drops would have resulted into an imperceptible deflection of the drop trajectories above the gauge collector.

The videos recorded by the camera were imported and analyzed in the MATLAB® environment. The methodology of detection of the drop position differs depending on the type of acquisition. At high frame rate, the path of each drop is identified by many frames: in every frame the drop is in a different position. Due to the reduced exposure time of each image, little light enters into the camera sensor and the image is dark. To improve the drop position identification, each image was then converted to greyscale and a combination of a Gaussian and Laplacian filter was applied. The image was binarized using a threshold level, with the zeroes indicating the background color while the ones indicate the drop. Finally, using a moving window over the image, the center of the drop was identified and stored. Knowing the time interval between two subsequent images and the conversion rate from pixels to mm, it was also possible to calculate the drop speed in the 2-D shooting plane. In low frame rate acquisition, due to the high exposure time, every frame appears much brighter and contains a streak representing the trajectory of each single drop. The same filtering and binarization operations were used, adapting the filter and threshold parameters. Finally, morphological operations were carried out to extract the middle line streak from the image, directly corresponding to the trajectory of the drop.

2.2. CFD Simulations

To obtain the disturbed airflow velocity fields (magnitude and components) around the two investigated gauges, CFD simulations were performed under constant wind velocity and uniform incoming free-stream conditions. First, an Unsteady Reynolds Average Navier-Stokes (URANS) model was applied to the simulation of the flow field around the Geonor T200B© gauge geometry to check the occurrence of any variation in time of the average velocity field. Results revealed that a steady state solution is reached in the region of major interest for this work, that is, above the gauge collector, and only beyond the gauge, in the wake, a time dependent solution persists. For this reason, to reduce the computational burden, a RANS model was used in the simulation of the Lambrecht Rain(e)H3© gauge. In both cases, the SST (Shear Stress Transport) k-ω turbulence model, based on the turbulence kinetic energy (k), the energy dissipation per unit mass (ε) and the turbulent specific dissipation rate (ω) as defined in Wilcox (2006), was adopted.

The SST k-ω closure model was developed by Menter (1993) and concentrates the advantages of the more classic k-ε and k-ω models because it can switch to a k-ε behaviour in the free stream far from the object and to the k-ω model near the walls. Indeed, the k-ε model formulated by Jones and Launder (1972), is robust and reliable in the free flow region but it proved to be unreliable near the boundary layer, while the k-ω model formulated by Wilcox (1988) is capable of correctly modeling turbulence near the boundary layer, though presenting a strong dependency on arbitrary values in the free flow. Concerning the topic of this work, Constantinescu et al. (2007) tested different numerical methods to investigate the shielding problem between two contiguous precipitation gauges and concluded that the SST k-ω model is more consistent with the time-dependent LES results on the upstream gauge, in conditions that are similar to the present work.

Although it was demonstrated (Cauteruccio et al., 2020) that the free-stream turbulence intensity inherent to the natural wind has a significant role in attenuating the aerodynamic effect of precipitation gauges, due to the energy dissipation induced by turbulent fluctuations, in this work a low free-stream turbulence

condition was used to suitably reproduce the WT environment where the particle tracking experiment was carried out.

To prepare the simulation setup, first the numerical models of the gauge geometries were realized in the Standard Triangulation Language (STL) format using a 3D CAD software. The three-dimensional computational spatial domains were discretized using an unstructured hybrid hexahedral/prismatic finite volume mesh. The number of cells of the computational mesh is 1.5×10^6 for the Geonor T200B$^{©}$ and doubled for the Lambrecht Rain(e)H3$^{©}$ due to the sharp edge that characterized the rim geometry, which requires an accurate discretization. In both cases, mesh refinement boxes and thin layers were realized close to the gauge and on its surface to increase the accuracy of the numerical solution in the region affected by large gradients of velocity and pressure. The quality of the mesh was checked by using the geometry parameters of orthogonality, skewness, and aspect ratio.

The open-source OpenFOAM software was employed to solve the URANS and RANS equations. The fluid air was modeled as a Newtonian incompressible fluid with kinematic viscosity $\nu_a = 1.5 \times 10^{-5}$ m^2 s^{-1} and density $\rho_a = 1.25$ kg m^{-3} at a reference environmental temperature $T_a = 20°C$. For each configuration, at the inlet of the computational domain (y-z plane) the undisturbed wind speed, U_{ref}, equal to 10 m s^{-1} was imposed parallel to the x axis and it was maintained uniform and constant in time, while a null gradient condition was set for pressure. At the outlet, y-z plane opposite to the inlet, the atmospheric pressure and a null gradient condition for the velocity were imposed. The lateral surfaces of the domain were set as symmetry planes, while the ground and the gauge surface were assumed impermeable with a no-slip condition. In all computational cells, initial conditions were imposed equal to U_{ref} for the velocity and equal to zero for the relative pressure.

This model was applied to the simulation of the airflow field generated in the WT. The aerodynamic behavior of the two precipitation gauges investigated was simulated and compared with the PIV and probe velocity measurements for validation purposes.

### 2.3. The Lagrangian Particle Tracking Model

The LPT model used by Colli et al. (2015) for solid precipitation was modified by introducing drag coefficient equations suitable for liquid precipitation. Drop trajectories were computed with a forward step procedure by calculating at short time intervals the particle position, velocity and acceleration. The relative particle-to-air velocity was updated at every time step by interpolating the CFD airflow field to obtain the flow velocity in the exact position of the drop. This model is one-way coupled since the potential influence of the particles on the airflow field is neglected. This simplification is acceptable since the particles concentration in the air is very low as observed by Cauteruccio (2020). A spherical shape was assumed for the water drops, with the associated equivalent diameter d, and the particle density was set equal to 1,000 kg m^{-3} at the air temperature of 20°C. The drag coefficient equations were implemented for various ranges of particle Reynolds number established a priori among those proposed in the literature by Folland (1988) and formulated starting from data published by Khvorostyanov and Curry (2005), hereinafter KC05.

The motion of particles when falling in the atmosphere is described by:

$$\rho_p V_p \boldsymbol{a}_p = -\frac{1}{2} C_D A_p \rho_a \left(\boldsymbol{v}_p - \boldsymbol{v}_a \right) \left| \boldsymbol{v}_p - \boldsymbol{v}_a \right| + V_p \left(\rho_p - \rho_a \right) \boldsymbol{g} \tag{1}$$

where $\boldsymbol{a}_p$ is the particle acceleration, $\boldsymbol{v}_a$ and $\boldsymbol{v}_p$ are the velocity vectors of the air and the particle, $\boldsymbol{g}$ is the gravity acceleration, C_D is the drag coefficient, A_p is the particle cross section area and ρ_a and ρ_p are the density of the air and the particle. Equation 1 assumes an upward positive orientation of the z axis, while the velocity and acceleration components are positive in the positive direction of the related axes. The quantity $\boldsymbol{v}_p - \boldsymbol{v}_a$ is the relative particle-to-air velocity.

The drag coefficient $\left(C_D \right)$ is a dimensionless quantity used to represent the aerodynamic resistance of an object in motion in a fluid, such as air or water, and depends on the cross-sectional area of the object $\left(A_p \right)$. The estimation of the drag coefficient is not easy. In the literature, different experiments were carried
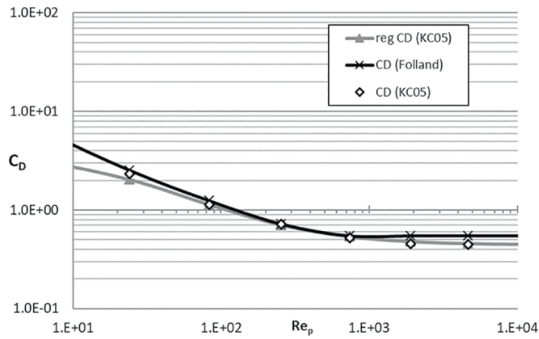
Figure 2. Comparison between the raw data proposed by KC05 (diamond), the best-fit curve of Equation 8 (gray line) and the formulation proposed by Folland (1988) (black line).

out with hydrometeors falling through the atmosphere with the objective of identifying suitable relationships between the drag coefficient and the particle dimension and/or its terminal velocity. Beard (1976) derived C_D by performing experiments in stagnant air and measuring the dimension d (mm) of the drops and their fall velocity w_T (m s^{-1}).

When a particle falls in a stagnant air its Reynolds number is expressed as:

$$Re_p = \frac{w_T d}{\upsilon_a} \tag{2}$$

where υ_a is the air viscosity in m^2 s^{-1}. The drag coefficient is directly related to the Reynolds number of the particle in motion. When a particle is immersed in a flow field the Equation 2 becomes a function of the particle-to-air velocity as follows:

$$Re_p = \frac{\left|\mathbf{v}_p - \mathbf{v}_a\right| d}{\upsilon_a} \tag{3}$$

Folland (1988) proposed different relationships between Re_p and C_D, for various ranges of Re_p (see Equations 4–7) and assumed that the minimum value for C_D must be fixed at 0.55.

$$Re_p < 0.01 \quad C_D = 2547 \tag{4}$$

$$0.01 \leq Re_p < 2 \quad C_D = 1.06\left(24\,Re_p^{-1} + 2.400\,Re_p^{-0.045}\right) \tag{5}$$

$$2 \leq Re_p \leq 21 \quad C_D = 1.06\left(24\,Re_p^{-1} + 2.640\,Re_p^{-0.190}\right) \tag{6}$$

$$21 < Re_p \quad C_D = 1.06\left(24\,Re_p^{-1} + 4.536\,Re_p^{-0.368}\right) \tag{7}$$

The equations proposed by Folland (1988) provide terminal velocities of raindrops in still air at the temperature of 7.5°C and atmospheric pressure that agree to within 2% with those of Mason (1971) over the range of terminal velocities $0.1 < w_T < 8.3$ m s^{-1}.

In the work of KC05, different formulations of C_D, as a function of Re_p obtained from experimental studies and analytical models, were summarized. Some of the curves proposed by KC05 are derived for spherical particles and other for crystals. The authors also introduce a correction, when the particle Reynolds number exceeds the value of 10^3, to account for the turbulence effect due to the flow.

The C_D values proposed by KC05 as a function of Re_p, for spherical particles in turbulent conditions, were fitted here for $Re_p > 60$ (approximately corresponding to a spherical drop of $d = 1$ mm falling in air, with $\upsilon_a = 1.5\ 10^{-5}$ m^2 s^{-1}, at an indicative fall velocity of 1 m s^{-1}) with an inverse first-order equation (Equation 8). The values of the three parameters are $y_0 = 0.442$, $a = 3.402$, $b = 21.383$ and the correlation factor (R^2) is equal to 0.996.

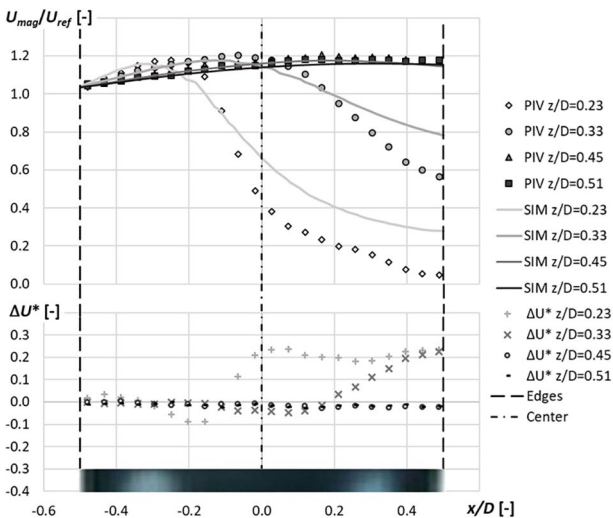$$C_D = y_0 + \frac{(ab)}{b + Re_p} \tag{8}$$

As shown in Figure 2, also the relationships proposed by Folland (1988) (black line) were compared with the raw data provided by KC05 (diamond). Based on this comparison the best-fit curve reported in Equation 8 (gray line in Figure 2) was implemented in the LPT model to calculate the drag coefficient for $Re_p > 400$, while the equations proposed by Folland (1988) were adopted for $Re_p \leq 400$.
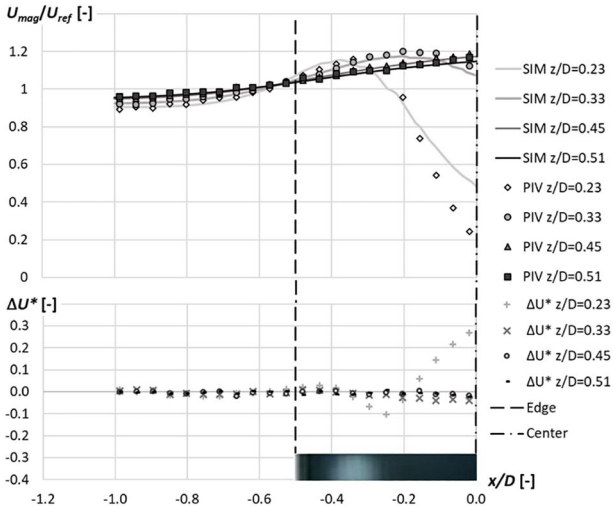
Figure 3. Comparison between simulated velocity profiles (continuous lines) and Particle Image Velocimetry measurements (markers) of the normalized magnitude of flow velocity (U_{mag}/U_{ref}) at $U_{ref} = 10$ m s^{-1} and at different elevations along the central plane ($y/D = 0$) (top panel) and their absolute difference ΔU^* (bottom panel) for the chimney gauge.

The LPT model was applied to the simulated airflow field to reproduce the trajectories of water drops as released in the WT. These were compared to the trajectories of the real drops detected by means of the video tracking system installed in the WT.

3. Results

3.1. CFD Simulation Results and Validation

CFD results are shown below in terms of normalized velocity profiles (continuous line) sampled in (x/D, z/D) planes at different crosswise coordinates (y/D). CFD profiles are compared with PIV and Cobra measurements indicated with markers for CH and CY gauges, respectively. In the first case their absolute difference (ΔU^*) is also reported, while for the Cobra measurements the uncertainty bars are depicted. For both simulation and WT results the term U_{ref} indicates the freestream velocity, while U_{mag} and U_z indicate the magnitude and vertical component of flow velocity, respectively. In the figures, a photograph of each gauge collector is inserted, colored black for the CH gauge and gray for CY gauge and the projection of the edges and the center of the collector are indicated with dashed and dash-dot lines, respectively.

Validation of the performed simulations was obtained in the WT using PIV and Cobra probe measurements for the CH and CY gauges, respectively.

A comparison between PIV measurements and CFD longitudinal profiles of the normalized magnitude of the flow velocity at $U_{ref} = 10$ m s^{-1}, for the CH gauge, is reported in Figure 3 and Figure 4. The plots refer to different elevations (z/D) and vertical sections, at $y/D = 0$ and $y/D = 0.25$, respectively, and the absolute difference (ΔU^*) between the measured and calculated values is also reported. The maximum differences occur at the minimum elevation where PIV measurements are available ($z/D = 0.23$ and 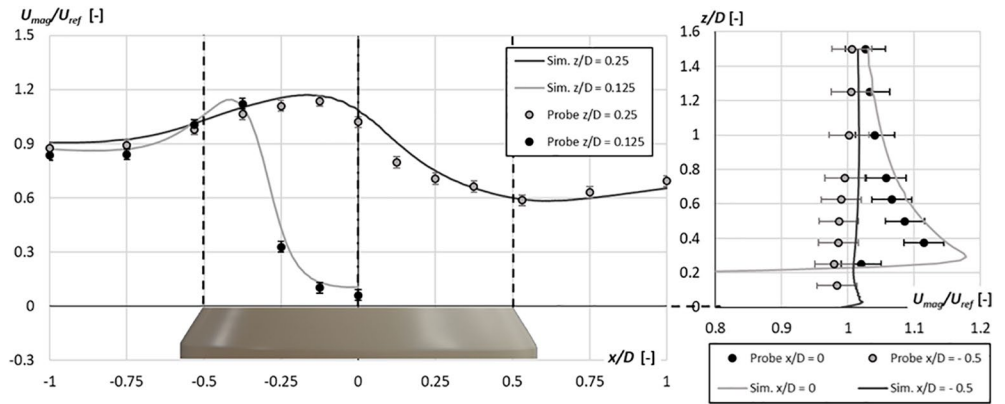0.33) and range between 0.2 and 0.3. Close to the gauge collector, indeed, the effect of the locally generated turbulence is more relevant, and the CFD model is less accurate in simulating turbulence fluctuations.

For the CY gauge, four velocity profiles were sampled by employing a Cobra probe above the collector, along the longitudinal symmetry plane of the gauge, in the (x/D, z/D) section at $y/D = 0$. A comparison between the Cobra probe velocity measurements (circles) and numerical results (solid lines) is shown in Figure 5. The longitudinal profiles were measured at $z/D = 0.125$ and $z/D = 0.25$, while the vertical profiles at the upwind edge and the center of the collector ($x/D = -0.5$ and $x/D = 0$, respectively). In all cases, the numerical profiles fall within the uncertainty of the probe measurements, depicted with bars.

3.2. Observation of the Deflected Trajectories

For the two investigated gauges, a few sets of drops captured in the GVPM when traveling above the gauge collector are shown in this section, and the observed trajectories are commented according to the aerodynamic response of the gauge body. Drop trajectories are depicted in the dimensionless plane (x/D, z/D), where the gauge collector is centered in (0, 0) and the longitudinal coordinate, x/D, of the drop releasing position is fixed, while its elevation, z/D (assumed positive downward), varies with

Figure 4. Comparison between simulated velocity profiles (continuous lines) and Particle Image Velocimetry measurements (markers) of the normalized magnitude of flow velocity (U_{mag}/U_{ref}) at $U_{ref} = 10$ m s^{-1} and at different elevations along the plane $y/D = 0.25$ (top panel) and their absolute difference ΔU^* (bottom panel) for the chimney gauge.

Figure 5. Comparison between simulated velocity profiles (continuous lines) and Cobra probe velocity measurements (circles with uncertainty bars) of the normalized magnitude of flow velocity (U_{mag}/U_{ref}) at $U_{ref} = 10$ m s^{-1} in the central plane ($y/D = 0$). Two longitudinal profiles at different elevations z/D (left-hand panel) and two vertical profiles at the upwind edge ($x/D = -0.5$) and at the center ($x/D = 0$) of the collector (right-hand panel) are shown for the cylindrical gauge.

the wind speed. In the legend, the prefix in the coding of each trajectory indicates the name of the gauge under test (G for GeonorT200B$^{©}$ and L for Lambrecht Rain(e)H3$^{©}$).
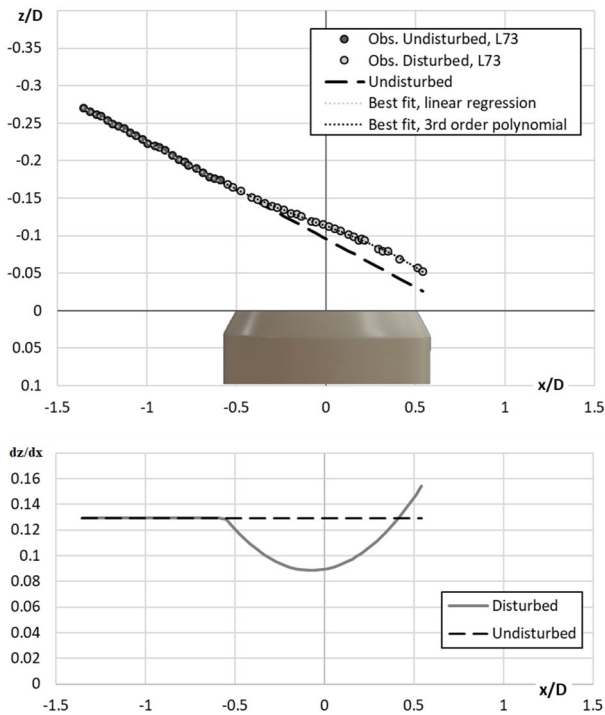
Overall, the experimental campaign in the WT resulted in the capturing of 82 trajectories of drops released between $z/D = -0.05$ and $z/D = -0.7$ above the CH gauge, at $U_{ref} = 8.86$–13.6 m s^{-1}, and 106 trajectories of drops released between $z/D = -0.18$ and $z/D = -0.7$ above the CY gauge at $U_{ref} = 8.9$–13.1 m s^{-1}. For both gauges, drop trajectories were shot at 10 and 1,000 fps.

Nineteen pairs of observed drop trajectories, for the two investigated gauge geometries, allowed to verify the repeatability of the experimental setup as demonstrated in the work of Cauteruccio, Brambilla, et al. (2021).
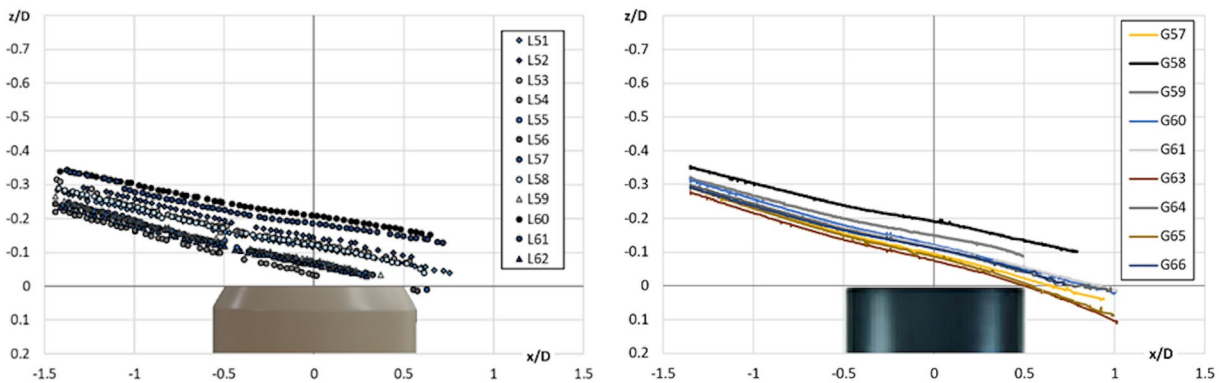
Two sample sets of drop trajectories shot at 1,000 and 10 fps are shown in Figure 6 (left and right panel, respectively), as observed above the collector of the CY and CH gauges at $U_{ref} = 12.5$ m s^{-1} and $U_{ref} = 11.4$ m s^{-1}, respectively. The particle-fluid interaction above the collector of the gauges is responsible for a significant deviation of the trajectories, and this can be observed here for all trajectories when traveling beyond the upwind edge of the collector ($x/D = -0.5$). In both cases, a few undisturbed trajectories aiming at entering the collector close to the downwind edge ($x/D = 0.5$) overtake its rim and fall outside of the gauge.

The estimated undisturbed trajectory is added in the top panel of Figure 7 (dashed line) for one sample drop traveling above the CY gauge at $U_{ref} = 12.5$ m s^{-1}. In this case, the observed trajectory starts detaching from the undisturbed one when its longitudinal coordinate reaches the upwind edge of the collector (at about $x/D = -0.5$), where the airflow updraft is most significant (as shown by Cauteruccio, Brambilla, et al., 2021).

Figure 6. Sample sets of drop trajectories shot at 1,000 (left) and 10 (right) fps, as observed above the collector of the cylindrical and chimney gauges at $U_{ref} = 12.5$ m s^{-1} and $U_{ref} = 11.4$ m s^{-1}, respectively.

The observed drop trajectory was elaborated by linearly interpolating the positions associated with the undisturbed part of the trajectory, while the disturbed part was fitted with a third order polynomial. In Figure 7 (top panel), the undisturbed part of the observed trajectory is painted in dark gray while the disturbed part is painted in light gray and the interpolation curves are marked with dots. The threshold between the undisturbed and

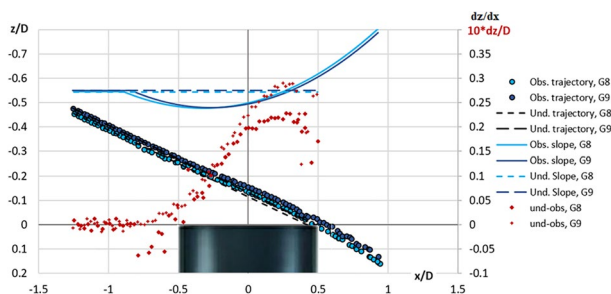**Figure 7.** Observed (circles) and undisturbed (dashed line) drop trajectory above the collector of the cylindrical gauge (top panel) at $U_{\mathrm{ref}} = 12.5$ m s^{-1}, and the associated slope curves for both trajectories (bottom panel).

disturbed part of the trajectory was obtained by adopting a trial-and-error procedure with the objective to ensure the continuity of the slope curve (dz/dx) obtained as the first derivative of the fitted trajectory (Figure 7, bottom panel).

Two drop trajectories, identified with the names G8 and G9, traveling above the collector of the CH gauge at $U_{\mathrm{ref}} = 10.2$ m s^{-1} are depicted in Figure 8. The initial elevation (z/D) of the two drops is not much different. The initial, undisturbed part of the slope curve reveals that the two drops have a similar size, while the drop starting at a higher elevation is deviated a bit later following the airflow pattern. The difference between the observed and undisturbed trajectories, red markers with scale on the right-hand axis, is larger in the second half part of the collector where the two drops are dragged beyond the gauge, resulting in some undercatch.

3.3. Validation of the Lagrangian Particle Tracking Model

The validation of the LPT model was obtained by comparison between observed and simulated trajectories. In the numerical model the initial conditions, normalized position (x/D and z/D) and velocity components (u and w [m s^{-1}], the latter assumed positive downward), of the simulated trajectories were set consistently with the WT observations. CFD airflow velocity fields were rescaled according to the free-stream velocity value used in the WT. The initial velocity components were set equal to the mean values of the three to five initial positions of each drop as shot by the camera, to avoid the noise due to the uncertainty in the initial positions. The drop diameter, d, which has a major role in the calculation of the drop trajectory by affecting Re_p and therefore C_D, is obtained here as a calibration parameter for each trajectory, since the drop releasing mechanism and the acquisition system cannot provide sufficient accuracy in the assessment of the drop size, while the use of other non-invasive drop size detectors was made difficult by the operating conditions in the WT.

A subset of about 25 observed drop trajectories is compared with the simulated ones in this section to support the validation phase. They were chosen in order to cover a variety of wind speed, drop size, initial drop velocity and position for each gauge geometry. The initial conditions of the nine drop trajectories visualised in this section and their estimated drop diameter are listed in Table 1.

Figure 8. Comparison of two drop trajectories (circles) having similar size, traveling above the collector of the chimney gauge at $U_{\mathrm{ref}} = 10.2$ m s^{-1}, together with the associated undisturbed trajectories (dashed lines). The associated slope curves (scale on the right-hand axis) are shown with colored solid and dashed lines for the disturbed and undisturbed trajectories, respectively. Red markers represent the difference between the observed and undisturbed trajectories in terms of normalized vertical coordinates (scale on the right-hand axis).
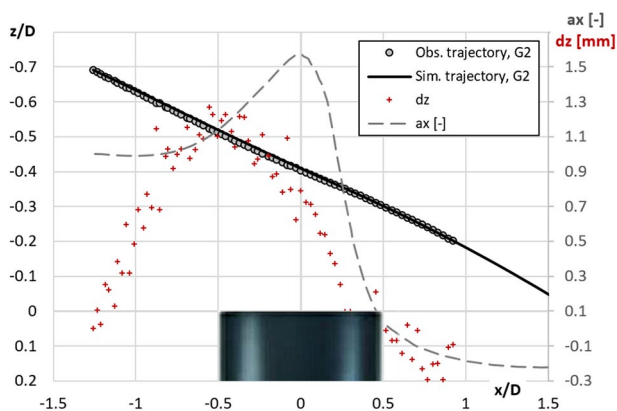
The observed (circles) and simulated (solid line) patterns of the drop trajectory identified with the name G2, are compared in Figure 9. The maximum difference between the vertical positions (z in mm), computed at each normalized longitudinal coordinate (x/D) of the observed trajectory, arises at the upwind edge of the collector and is about 1.2 mm. This difference is comparable with the drop size (see Table 1), therefore with the uncertainty in the assessment of the drop position, identified as a bright

Table 1
WT Flow Velocity, Initial Coordinates and Velocity Components for the Simulated Drop Trajectories and the Resulting Drop Diameter

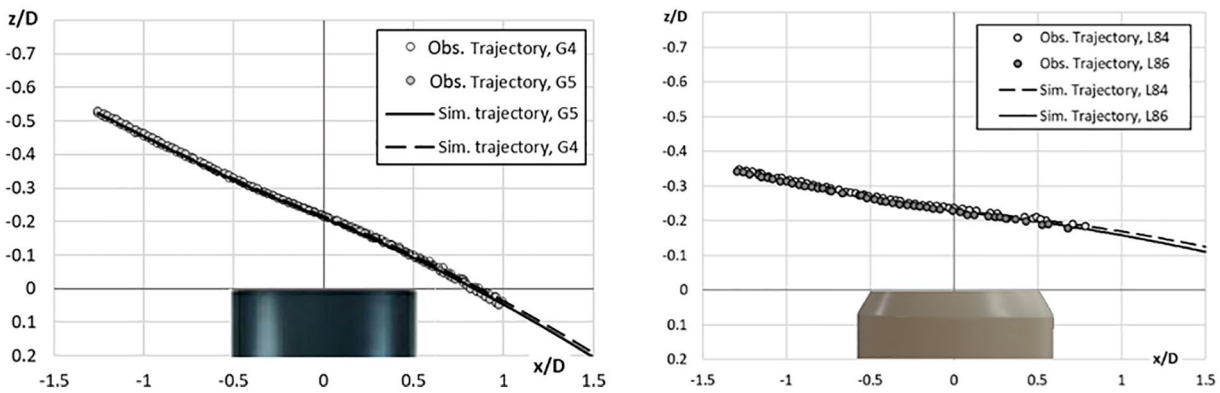| ID	Wind (m s^{-1})	x/D	z/D	u (m s^{-1})	w (m s^{-1})	d (mm)
G2	10.2	−1.259	−0.690	4.286	0.952	1.2
G4	10.2	−1.257	−0.523	4.140	1.104	1.0
G5	10.2	−1.257	−0.523	4.122	1.122	1.0
G8	10.2	−1.247	−0.455	4.048	1.190	1.0
G9	10.2	−1.256	−0.477	3.968	1.190	1.0
L84	13.1	−1.280	−0.349	5.571	0.667	0.7
L86	13.1	−1.293	−0.343	5.801	0.602	0.7
L97	13.1	−1.392	−0.389	5.855	0.482	0.7
L100	13.1	−1.379	−0.393	5.667	0.524	0.9

moving object in each frame. The calculated horizontal acceleration of the drop, normalized with the one experienced in the initial undisturbed part of the trajectory, is also shown (scale on the right-hand axis). Consistently with the PIV airflow velocity fields, the drop significantly accelerates when traveling above the upwind part of the collector, where the airflow is indeed accelerated, until crossing the separation layer between the airflow recirculation and accelerated zones, when it starts decelerating abruptly toward the downwind edge of the collector.

The good repeatability of the trajectories of very similar drops in the WT (see their estimated size in Table 1) is shown in Figure 10. By injecting drops of the same size in the WT, the observed trajectories are indeed very close to each other, and they experience very similar deviations above the collector. Moreover, simulated trajectories show that the LPT model is able to replicate even the small variations due to slight differences in the initial conditions about the drop velocity.

The observed drop trajectories G8 and G9, already shown in Figure 8, are compared with the simulated trajectories in Figure 11. As already noted, the two drops have the same size; this assumption is confirmed by the obtained numerical trajectories because the optimal agreement between the observed and simulated trajectories is reached by setting the drop diameter equal to one millimeter. Again, the difference between observed and simulated trajectories is comparable with the uncertainty in the assessment of the drop position, given the dimension of the drop (see Table 1) and the image resolution. The vertical acceleration of the drops (a_z) obtained from the simulation, normalized with the one experienced in the initial undisturbed part of the trajectory, is depicted with dashed lines: the two drops accelerate when reaching the upwind edge of the collector, due to the updraft, and then decelerate. This behavior is in line with the measured PIV velocity field where, beyond $x/D = -0.25$, the updraft zone is always located above the normalized elevation $|z/D| = 0.2$ and the two drops are fully immersed in the recirculation zone.

Observed and simulated patterns are depicted in Figure 12 for a pair of drop trajectories (named L97 and L100) having different drop size ($d = 0.7$ and 0.9 mm) but being released at the same initial position. As reported in Table 1, also the values of the initial velocity components are very similar. The smaller drop has a lower slope and is maintained at a higher elevation along the entire trajectory. As revealed by the PIV velocity field, this is due to the persistence of updraft velocity components above $|z/D| = 0.25$ within the limits of the collector, while below this vertical coordinate the separation layer occurs, and downward vertical velocity components arise.

Validation of the coupled CFD and LPT approach was obtained after numerically simulating about 25 trajectories of drops released in the WT experiment. A synthesis of the validation performance is reported in Table 2. The maximum, mean and median difference, dz, between the vertical coordinates along each observed and simulated trajectory, normalized with the estimated drop diameter, d, were calculated as suitable performance parameters. For each of them, the maximum, minimum, mean and standard deviation values obtained over the set of all trajectories used in the validation exercise are listed in Table 2. The same statistics are included for the root mean square difference between the observed and simulated vertical coordinates along each trajectory.

The validation was satisfactory since the mean of the maximum normalized differences between the simulation and the observed trajectory is about unity, with a low standard deviation (the coefficient of variation is about 0.4). Also, the mean and median values of dz are very similar, showing a symmetrical spread of these differences around the perfect agreement, which

Figure 9. Observed (circles) and simulated (solid line) drop trajectories above the collector of the chimney gauge at $U_{ref} = 10.2$ m s^{-1}. The difference dz (mm) between the observed and simulated vertical coordinates of the drop trajectories (red crosses) at each normalized observed longitudinal coordinate (x/D) is reported (scale on the right-hand axis), together with the numerical longitudinal acceleration (a_x) of the drop (dashed line).

Figure 10. Pairs of drops having approximately the same size traveling above the collector of the chimney gauge at $U_{ref} = 10.2$ m s^{-1} (left-hand panel) and cylindrical gauge at $U_{ref} = 13.1$ m s^{-1} (right-hand panel). Observed (circles) and simulated (lines) trajectories are depicted for the two pairs of drops.

suggests quite a random nature of the error. Finally, the RMSD is very low, always below 10^{-3}, indicating an overall good agreement for all pairs of simulated and observed trajectories.

4. Discussion

Although the experimental conditions implemented in the WT tests were forcedly different from reality (constant and low turbulence airflow), and the initial conditions of the drops at their releasing position were different from those expected in the natural environment (null horizontal and vertical velocity instead of the free-stream and terminal velocity, respectively), the performed validation of the coupled CFD and LPT approach on a physical full-scale model in the WT supports its application in realistic simulation scenarios.

The diameter of drops generated in this work ranges between 0.7 and 1.2 mm. Although they do not span over the entire range of the typical rain drop size in nature, such drops account for about 27%–33% of the total number of drops and 37% to 20% of the total water volume, in the observed Drop Size Distribution (DSD) of real rainfall events for rain intensity classes from light (<1 mm/h) to intense (>20 mm/h) events (see Caracciolo et al., 2008). Most of the remaining drop would have a smaller diameter.

The generated drops are also assumed to be spherical, and the associated drag coefficient used in the simulation is that typical of spherical drops, although large drops are oblate in nature due to the resistance of air to the falling movement of the drop. Drops start to be significantly oblate at a diameter slightly larger than 2 mm (axis ratio b/a = 0.90 according to Beard & Chuang, 1987). Drops smaller than 2 mm account for about 99%–97% of the total number of drops and for 85%–62% of the total water volume, depending on the same rainfall intensity classes reported by Caracciolo et al. (2008). Therefore, the performed experiments are representative of most part of the DSD of real rainfall events and, most importantly, precisely of that portion of the DSD that is strongly influenced by the aerodynamic behavior of the gauge (large drops are more inertial and do not change their trajectory significantly in windy conditions).
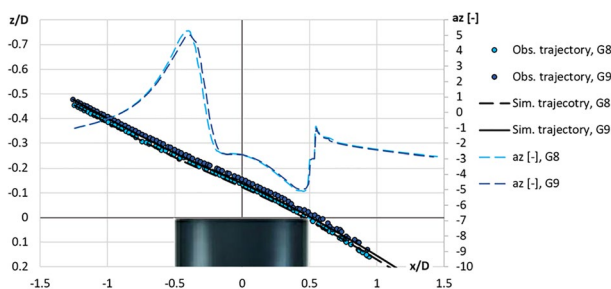
Figure 11. Comparison of two simulated and observed trajectories for two drops traveling above the collector of the chimney gauge at $U_{ref} = 10.2$ m s^{-1}, together with the simulated profiles of their normalized vertical acceleration (scale on the right-hand axis).

The performed CFD simulations confirmed previous literature results (e.g., Cauteruccio, 2020; Colli et al., 2018): the airflow accelerates above the collector of the investigated gauges and significant updraft is obtained just in front of the gauge collector and above it. The region of maximum acceleration for the CH gauge shows higher values and is larger and more dispersed upward if compared with the aerodynamic response of the CY gauge. The maximum normalized updraft U_z/U_{ref} occurs above the upwind edge of the collector and, for example, at $z/D = 0.125$ it equals 0.65 and 0.50 (against the expected null value) for the CH and CY gauge, respectively. These airflow features are the most influential on the hydrometeor trajectories, which are deflected upward due to the updraft and tend to be dragged beyond the collector when falling through the
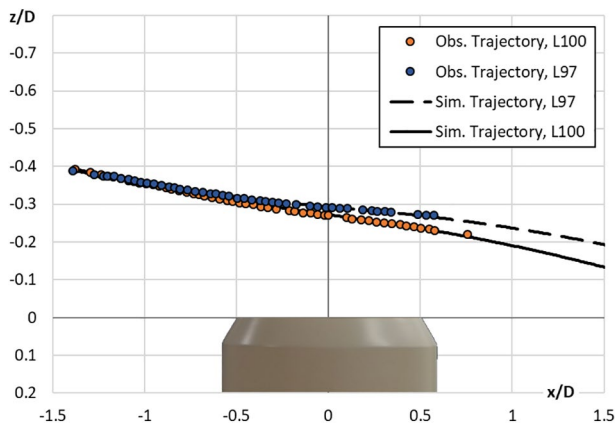
Figure 12. Observed (circles) and simulated (lines) drop trajectories for two drops of different size, released at the same initial position and traveling above the collector of the cylindrical gauge at $U_{\text{ref}} = 13.1$ m s^{-1}.

accelerated zone, where the horizontal velocity is larger than the undisturbed wind speed.

For the CH gauge the validation of CFD simulation results was obtained by comparison with PIV measurements. An overall good agreement of the simulated profiles with measurements was obtained. The maximum absolute differences (ΔU^*) obtained at the minimum elevation ($z/D = 0.23$) are due to the coarse discretization of the measured spatial domain, which introduces a smoothing effect on the measured flow field. Moreover, close to the gauge, measurements are still slightly affected by the reflection of the laser beam on the gauge rim, partially concealing the passive tracer from detection despite a mask was implemented to reduce such effect.

For the CY gauge the numerical profiles were compared with Cobra measurements. In all cases the velocity profiles fall within the uncertainty of the probe measurements confirming the good quality of the adopted CFD setup. The adoption of two different WT approaches to validate the CFD setup can be considered as a strong point of the present work.

The video shooting of the deviated trajectories in the WT allowed clear visualization of the wind-induced undercatch by showing that some drops actually fall outside instead of inside of the collector, contrary to what would be expected by following their undisturbed trajectory. Validation of the coupled CFD and LPT approach was obtained by comparing simulated and observed drop trajectories under the same initial and boundary conditions as demonstrated by the statistics of the performance parameters summarized in Table 2.

Note that the LPT model is fully deterministic, therefore there would be limited added value in validating the model with a large number of very similar trajectories. The chosen trajectories are on the contrary representative of different drop dynamics due to the varied initial, microphysical and boundary conditions.

5. Conclusions

Previous works on wind-induced errors mostly concentrated on field studies (see e.g., Buisán et al., 2017 and Kochendorfer et al., 2017 for both liquid and solid precipitation) based on the comparison of measurements obtained from shielded and unshielded gauges. Adjustment curves (also termed transfer functions) are usually derived from field data alone, assuming some gauge/windshield configuration as a reference. Limitations of the empirical approach include the high variability of the hydrometeor microphysical characteristics in precipitation events (Thériault et al., 2012), as well as the possible wind-induced biases associated with the reference configuration (Thériault et al., 2015). The resulting large spread of field data around the interpolating curves suggests that important driving factors are understated, such as precipitation intensity and/or the particle size distribution, as recently shown by Colli et al. (2020).

The present work overcomes these existing gaps, shedding additional light on the wind exposure problem, with results that can be used operationally to adjust precipitation measurements obtained in windy conditions. Indeed, the WT validation of the numerical approach based on CFD and LPT simulations supports its use as the theoretical basis for the interpretation of the wind-induced bias of field measurements obtained from shielded and unshielded precipitation gauges. Field measurements from suitable test sites, equipped with reference gauges in the appropriate configuration, remains essential to provide the real-world test bench and calibration basis needed to confirm the parameterization adopted (e.g., for the drag coefficient) in the theoretical approach.

Typical applications include the numerical calculation of the collection efficiency of precipitation gauges having different outer geometries

Table 2
Validation Statistics for the Selected Performance Parameters

	Max (dz/d)	Mean (dz/d)	Median (dz/d)	RMSD
Max	2.1492	1.0444	1.2154	0.000812
Min	0.1871	−0.4230	−0.4946	0.000213
Mean	1.0968	0.0332	0.0337	0.000429
Std dev	0.4351	0.3514	0.3905	0.000168

(based on suitable assumptions and/or ancillary measurements about the hydrometeor characteristics, drag coefficient and drop size distribution). Adjustment curves for the wind-induced bias of precipitation measurements can be therefore derived to be used operationally for correcting the raw measurements (Cauteruccio & Lanza, 2020).

Also, this work may help investigating the propagation of measurement biases into the modeling of hydrological processes, especially in the field of water resources assessment, by validating a suitable simulation framework. Fully validated simulations are indeed precious to quantify the impact of wind-induced errors on the estimation of rain fields used as an input to hydrological models operating at the natural catchment scale.

Additionally, knowledge of the wind-induced biases of ground-based measurement instruments supports a better understanding of the reliability of remotely sensed estimates of the rain field from satellite sensors, which provide the necessary information about areal precipitation over large regions, and of the uncertainty of radar-based rainfall retrieval.

Both such aspects were the focus of an Italian national project entitled "Reconciling precipitation with runoff: the role of understated measurement biases in the modeling of hydrological processes," which raised the need for the present research.

Data Availability Statement

The coordinates of the observed drop trajectories used in this work are available online at: http://www.precipitation-biases.it/Drop-Trajectories-WRR.php.

References

Beard, K. V. (1976). Terminal velocity and shape of cloud and precipitation drops aloft. *Journal of the Atmospheric Sciences*, *33*, 851–864. https://doi.org/10.1175/1520-0469(1976)033%3C0851:TVASOC%3E2.0.CO;2

Beard, K. V., & Chuang, C. (1987). A new model for the equilibrium shape of raindrops. *Journal of the Atmospheric Sciences*, *44*(11), 1509–1524. https://doi.org/10.1175/1520-0469(1987)044%3C1509:ANMFTE%3E2.0.CO;2

Buisán, S. T., Earle, M. E., Collado, J. L., Kochendorfer, J., Alastrué, J., Wolff, M., et al. (2017). Assessment of snowfall accumulation underestimation by tipping bucket gauges in the Spanish operational network. *Atmospheric Measurement Techniques*, *10*, 1079–1091. https://doi.org/10.5194/amt-10-1079-2017

Caracciolo, C., Porcù, F., & Prodi, F. (2008). Precipitation classification at mid-latitudes in terms of drop size 488 distribution parameter. *Advances in Geosciences*, *16*, 11–17. https://doi.org/10.5194/adgeo-16-11-2008

Cauteruccio, A. (2020). The role of turbulence in particle-fluid interaction as induced by the outer geometry of catching-type precipitation gauges. (Ph.D. Thesis). Ph.D. course in Civil, Chemical and Environmental Engineering, curriculum in Fluid Dynamics and Environmental Engineering. University of Genova. https://doi.org/10.15167/cauteruccio-arianna_phd2020-04-06

Cauteruccio, A., Brambilla, E., Stagnaro, M., Lanza, L. G., & Rocchi, D. (2021). Experimental evidence of the wind-induced bias of precipitation gauges using Particle Image Velocimetry and particle tracking in the wind tunnel. In press on *Journal of Hydrology*. https://doi.org/10.1016/j.hydroa.2021.100081

Cauteruccio, A., Chinchella, E., Stagnaro, M., & Lanza, L. G. (2021). Snow particle collection efficiency and adjustment curves for the hotplate precipitation gauge. *Journal of Hydrometeorology*, *22*(4), 941–954. https://doi.org/10.1175/JHM-D-20-0149.1

Cauteruccio, A., Colli, M., Freda, A., Stagnaro, M., & Lanza, L. G. (2020). The role of free-stream turbulence in attenuating the wind updraft above the collector of precipitation gauges. *Journal of Atmospheric and Oceanic Technology*, *37*(1), 103–113. https://doi.org/10.1175/JTECH-D-19-0089.1

Cauteruccio, A., & Lanza, L. G. (2020). Parameterization of the collection efficiency of a cylindrical catching-type rain gauge based on rainfall intensity. *Water*, *12*(12), 3431. https://doi.org/10.3390/w12123431

Colli, M., Lanza, L. G., Rasmussen, R., & Thériault, J. M. (2016a). The collection efficiency of shielded and unshielded precipitation gauges. Part I: CFD airflow modelling. *Journal of Hydrometeorology*, *17*, 231–243. https://doi.org/10.1175/JHM-D-15-0010.1

Colli, M., Lanza, L. G., Rasmussen, R., & Thériault, J. M. (2016b). The collection efficiency of unshielded precipitation gauges. Part II: Modeling particle trajectories. *Journal of Hydrometeorology*, *17*, 245–255. https://doi.org/10.1175/JHM-D-15-0011.1

Colli, M., Lanza, L. G., Rasmussen, R., Thériault, J. M., Baker, B. C., & Kochendorfer, J. (2015). An improved trajectory model to evaluate the collection performance of snow gauges. *Journal of Applied Meteorology and Climatology*, *54*, 1826–1836. https://doi.org/10.1175/JAMC-D-15-0035.1

Colli, M., Pollock, M., Stagnaro, M., Lanza, L. G., Dutton, M., & O'Connell, P. E. (2018). A Computational Fluid-Dynamics assessment of the improved performance of aerodynamic raingauges. *Water Resources Research*, *54*, 779–796. https://doi.org/10.1002/2017WR020549

Colli, M., Stagnaro, M., Theriault, J. M., Lanza, L. G., & Rasmussen, R. (2020). Adjustments for wind-induced undercatch in snowfall measurements based on precipitation intensity. *Journal of Hydrometeorology*, *21*(5), 1039–1050. https://doi.org/10.1175/JHM-D-19-0222.1

Constantinescu, G. S., Krajewski, W. F., Ozdemir, C., & Tokyay, T. (2007). Simulation of airflow around rain gauges: Comparison of LES with RANS models. *Advances in Water Resources*, *30*, 43–58. https://doi.org/10.1016/j.advwatres.2006.02.011

Folland, C. K. (1988). Numerical models of the raingauge exposure problem, field experiments and an improved collector design. *Quarterly Journal of the Royal Meteorological Society*, *114*, 1485–1516. https://doi.org/10.1002/qj.49711448407

Green, M. J., & Helliwell, P. R. (1972). The effect of wind on the rainfall catch. Distribution of precipitation in mountainous areas. *World Meteorological Organization Report 326*, *2*, 27–46.

Habib, E. H., Meselhe, E. A., & Aduvala, A. V. (2008). Effect of local errors of tipping-bucket rain gauges on rainfall-runoff simulations. *Journal of Hydrologic Engineering*, *13*(6), 448–496. https://doi.org/10.1061/(ASCE)1084-0699(2008)13:6(488)

Jevons, W. S. (1861). On the deficiency of rain in an elevated rain-gauge, as caused by wind. *The London, Edinburgh, and Dublin Philosophical Magazine and Journal of Science*, *21*(4), 421–433. https://doi.org/10.1016/0016-0032(62)90997-3

Jones, W. P., & Launder, B. E. (1972). The prediction of laminarization with a two-equation model of turbulence. *International Journal of Heat and Mass Transfer*, *15*, 301–314. https://doi.org/10.1016/0017-9310(72)90076-2

Khvorostyanov, V. I., & Curry, J. A. (2005). Fall velocities of hydrometeors in the atmosphere: Refinements to a continuous analytical power law. *Journal of the Atmospheric Sciences*, *62*, 4343–4357. https://doi.org/10.1175/JAS3622.1

Kochendorfer, J., Nitu, R., Wolff, M., Mekis, E., Rasmussen, R., Baker, B., et al. (2017). Analysis of single-Alter-shielded and unshielded measurements of mixed and solid precipitation from WMOSPICE. *Hydrology and Earth System Sciences*, *21*(7), 3525–3542. https://doi.org/10.5194/hess-21-3525-2017

La Barbera, P., Lanza, L. G., & Stagi, L. (2002). Tipping-bucket mechanical errors and their influence on rainfall statistics and extremes. *Water Science and Technology*, *45*(2), 1–9. https://doi.org/10.2166/wst.2002.0020

Lanza, L. G., & Stagi, L. (2008). Certified accuracy of rainfall data as a standard requirement in scientific investigations. *Advances in Geosciences*, *16*, 43–48. https://doi.org/10.5194/adgeo-16-43-2008

Mason, B. J. (1971). *The physics of clouds* (2nd ed.), Clarendon Press (ISBN: 9780199588046).

Menter, F. (1993). Zonal two equation k-ω turbulence models for aerodynamic flows. *AIAA 24th Fluid Dynamics Conference, 93*, p.2906. https://doi.org/10.2514/6.1993-2906

Molini, A., Lanza, L. G., & La Barbera, P. (2005). The impact of tipping bucket measurement errors on design rainfall for urban-scale applications. *Hydrological Processes*, *19*(5), 1073–1088. https://doi.org/10.1002/hyp.5646

Mueller, C. C., & Kidder, E. H. (1972). Rain gage catch variation due to airflow disturbances around a standard rain gage. *Water Resources Research*, *8*(4), 1077–1082. https://doi.org/10.1029/WR008i004p01077

Nešpor, V., & Sevruk, B. (1999). Estimation of wind-induced error of rainfall gauge measurements using a numerical simulation. *Journal of Atmospheric and Oceanic Technology*, *16*(4), 450–464. https://doi.org/10.1175/1520-0426(1999)016%3C0450:EOWIEO%3E2.0.CO;2

Rasmussen, R., Vivekanandan, J., Cole, J., Masters, B. M. C., & Masters, C. (1999). The estimation of snowfall rate using visibility. *Journal of Applied Meteorology*, *38*(10), 1542–1563. https://doi.org/10.1175/1520-0450(1999)038%3C1542:TEOSRU%3E2.0.CO;2

Robinson, A. C., & Rodda, J. C. (1969). Rain wind and aerodynamic characteristics of rain-gauges. *The Meteorological Magazine*, *98*, 113–120.

Thériault, J. M., Rasmussen, R., Ikeda, K., & Landolt, S. (2012). Dependence of snow gauge collection efficiency on snowflake characteristics. *Journal of Applied Meteorology and Climatology*, *51*, 745–762. https://doi.org/10.1175/JAMC-D-11-0116.1

Thériault, J. M., Rasmussen, R., Petro, E., Trépanier, J. Y., Colli, M., & Lanza, L. G. (2015). Impact of wind direction, wind speed, and particle characteristics on the collection efficiency of the double fence intercomparison reference. *Journal of Applied Meteorology and Climatology*, *54*(9), 1918–1930. https://doi.org/10.1175/JAMC-D-15-0034.1

Valík, A., Brázdil, R., Zahradnícek, P., Tolasz, R., & Fiala, R. (2021). Precipitation measurements by manual and automatic rain gauges and their influence on homogeneity of long-term precipitation series. *International Journal of Climatology*, *41*(1), E2537–E2552. https://doi.org/10.1002/joc.6862

Warnik, C. C. (1953). Experiments with windshields for precipitation gages. *Transactions - American Geophysical Union*, *34*(3), 379–388. https://doi.org/10.1029/TR034i003p00379

Wilcox, D. C. (1988). Reassessment of the scale-determining equation for advanced turbulence models. *AIAA Journal*, *26*(11), 1299–1310. https://doi.org/10.2514/3.10041

Wilcox, D. C. (2006). *Turbulence modeling for CFDD C W industries* (3rd ed.).